TUDelft

Delft University of Technology

Coarsening of foam in two model fractures with different roughness

Li, Kai; Sharifnik, Mohammadamin; Wolf, Karl Heinz A.A.; Rossen, William R.

Important note
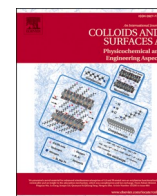To cite this publication, please use the final published version (if applicable).
Please check the document version above.

Coarsening of foam in two model fractures with different roughness

Kai Li [a],[*],[1], Mohammadamin Sharifnik [b], Karl-Heinz A.A. Wolf [a], William R. Rossen [a]

[a] Department of Geoscience & Engineering, Delft University of Technology, the Netherlands
[b] Department of Environment, Land and Infrastructure, Polytechnic University of Turin, Italy

HIGHLIGHTS

- Model fractures with roughed surface are represented by a network of pore bodies and throats.
- Foam images were processed to study bubble texture and quantify coarsening process.
- Lamellae height is estimated to study the mechanisms that may slow or stop the coarsening.
- How water saturation and capillary pressure affect foam coarsening is explained.

GRAPHICAL ABSTRACT
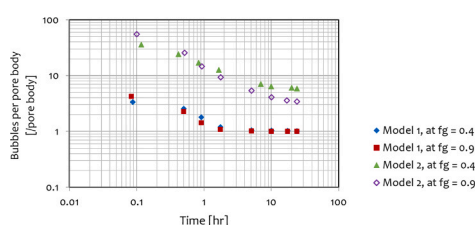
Fracture Model 1: regular roughness, hydraulic aperture of 46 μm
Fracture Model 2: irregular roughness, hydraulic aperture of 78 μm

ARTICLE INFO

ABSTRACT

Foam coarsening by diffusion (Ostwald ripening) has been well studied in bulk foams. However, it is less well understood in porous media. In particular, the mechanisms that may slow or stop coarsening have not been fully investigated. In this paper, we report an experimental study of foam coarsening in two 1-m-long and 15-cm-wide model fractures. The model fractures, Model 1 and Model 2, are made of glass plates and have different roughness. Model 1 has a regular roughness with hydraulic aperture of 46 μm. Model 2 has an irregular roughness with hydraulic aperture of 78 μm. The two model fractures are transparent, which allows direct investigation of foam in the fractures. We characterize the fracture geometries by studying the aperture distribution in the two model fractures. Both model fractures are then represented by a 2D network of pore bodies and pore throats. To study coarsening, we inject pre-generated foam at different foam qualities (ratio of gas volumetric rate to total rate) into the model fractures. After foam reaches steady-state, we shut the inlet and outlet valves of the fractures for 24 h. Foam coarsens by gas diffusion during this period. We use a high-speed camera to record images of the static foam during coarsening at two fixed locations in the fracture: 19 and 73 cm from the inlet, separately. We then use ImageJ software to process the images to study foam texture and quantify coarsening process. By correlating the aperture histogram of model fractures and water-occupied area fraction, we estimate the local aperture at water-gas interfaces at each specific coarsening time. Using the local aperture, we further estimate the height of lamellae available for gas diffusion at the end of the coarsening experiments. Based on this information, we discuss whether coarsening stops at the end of the coarsening experiments because bubbles are in equilibrium in pressure, or slows nearly to a stop because bubbles lose contact through lamellae. Coarsening studies in bulk and microfluidics assume coarsening slows and stops when lamella curvature is zero. We show in our model fractures that the lack of lamellae in wet foams can also play a part. In addition, we adopt

* Correspondence to: Department of Geoscience & Engineering, Stevinweg 1, 2628 CN Delft, the Netherlands.
  E-mail address: K.Li-2@tudelft.nl (K. Li).
[1] ORCID: 0000-0002-9592-2416.

a novel technique to calculate water saturation and capillary pressure of foam in our model fractures. We then explain how these foam properties affect its coarsening behavior.

Nomenclature

d_a	Local aperture at water-gas interfaces at a specific coarsening time
d_H	Hydraulic aperture of the model fracture
d_{throat}	Typical pore throat aperture of the model fractures
f_g	Foam quality (ratio of gas volumetric injection rate to total rate)
$L_{lamella}$	Total length of lamellae in the image
P_c	Capillary pressure
q_w	Volumetric water injection rate
V_{Pb}	Water volume in Plateau borders
w	Width of the model fracture
γ_s	Surface tension of the surfactant solution to air at 20 °C
θ	Contact angle
μ_w	Viscosity of water
∇P_w	Pressure gradient of water flow

1. Introduction

Aqueous foam comprises gas bubbles separated by continuous liquid films. The films are called lamellae and are stabilized by surfactant [1]. Foam has many applications in underground resources, such as aquifer remediation [2], acid stimulation [3], and enhanced oil recovery [4,5].

In enhanced oil recovery (EOR), gas injection usually suffers from poor sweep efficiency and leaves much oil behind because of sweep-efficiency problems such as gravity override, viscous fingering and channeling [6]. This is because gas has lower density and viscosity compared to in-situ fluids, and tends to flow preferably through high-permeability zones in heterogeneous reservoirs. Foam has been used to mitigate these sweep-efficiency problems for decades in EOR [5, 7–9]. During foam injection, foam can maintain a stable displacement front by reducing the mobility of the injected gas by a factor of hundreds or more, hence improving the sweep and increasing oil recovery [4,10]. To achieve an optimized mobility control, the stability of foam must be maintained while it propagates deep into the reservoir. In porous media, foam with a finer texture (smaller bubbles) and a larger bubble density gives a greater reduction of gas mobility, because its higher lamella density per unit of length gives a greater resistance on the flow [11]. However, at the pore scale, foam coalescence can take place due to different mechanisms including capillary coalescence and diffusive coarsening. Coarsening reflects gas diffusion between foam bubbles that are not in pressure equilibrium. It can alter the structure of foam and weaken its ability of gas reduction. Therefore, it is important to understand coarsening in order to predict foam behavior.

Foam coarsening by diffusion (Ostwald ripening) has been well studied in the context of bulk foam [12–15]. By considering mean number of faces per bubble, the classical von Neumann law is adopted to describe coarsening behavior in bulk foams [16]. In bulk foams, coarsening usually interferes with drainage, enhancing the drainage velocity [17]. Hilgenfeldt et al. [18] studied the coupling effects of these two mechanisms on foam evolution. They found that strong coarsening led to drainage times that were shorter and independent of the initial liquid content. They also incorporated the physics of both diffusive coarsening and drainage in their model and showed quantitative agreement with experiments. However, foam coarsening is less well understood in porous media. In porous media, foam bubbles rapidly attain a size close

to or bigger than pore body. Plateau borders form where lamellae meet the walls. Gas can diffuse much faster through thin lamellae than through Plateau borders or bulk water. Marchalot et al. [19] studied foam coarsening in a microfluidic system (length × width × height: 2500 × 1500 × 40 μm). They found that a typical time of foam ageing was about 2–3 min for polydisperse foam. The typical time would increase as the polydispersity of foam bubbles decreases. They showed that most diffusion occurred through lamellae and the lamella height was about one-tenth of the height of the system. Jones et al. [20] also investigated coarsening behavior in a microfluidic model (length × width × height: 6000 × 800 × 5 μm). They observed three coarsening regimes. Bubble size (2D average bubble area) of foam grew linearly with time at the beginning of coarsening. The coarsening rate then decreased as the effects of wall constraints became significant. The coarsening finally stopped after around half an hour, with the majority of lamellae located in pore throats, where lamella curvature was close to zero.

In this study, we conduct experiments to further investigate how foam evolves during coarsening by gas diffusion in porous media approximating the geometry of a narrow natural fracture in a geological formation. To this end, we build two glass-plate model fractures with different roughness and hydraulic apertures (46 μm and 78 μm, respectively) to represent geological porous media [21]. Unlike microfluidic models with uniform depth of etching [22,23], our model fractures each represents an open slit-like channel and has a distribution of continuously varied apertures over space. They are analogous to a 2D network of pore bodies (locations with wide aperture) and pore throats (locations with narrower aperture, connecting pore bodies). We characterize the fracture geometry of our models by studying their roughness. To study coarsening, we inject pre-generated foam into the model fractures and shut in the fractures after foam flow reaches steady-state. Foam then coarsens once it stops flowing in the fractures. As our models are transparent, we directly visualize foam coarsening in the fractures by using a fast-speed camera. Using ImageJ software, we analyze foam images to study how foam evolves during coarsening in the fractures. In particular, we study how coarsening affects foam texture and lamella location. In addition, we use a novel technique of image analysis to estimate water saturation and capillary pressure of foam [24]. We also estimate the height of lamellae through which gas can diffuse, and discuss how it relates to coarsening behavior.

2. Experimental setup and materials

Fig. 1 shows our experimental setup. We use a dual-cylinder pump (VINDUM Engineering, INC., Model VP1–12K™, range: 0–28 mL/min) to inject liquid, and a mass-flow controller (Bronkhorst Nederland B.V., F-230M™, range: 0.19–10 mL/min) to inject gas. A mixing tee with a frit filter inside (Upchurch Scientific, PEEK™, mesh size of the frit: 10 μm) is installed upstream of the inlet of the fracture to pre-generate foam. Two absolute-pressure sensors (DEMO MPXH6400A, range: 4 bar, accuracy: ±10 mbar) are mounted on the fracture to measure pressures at the inlet and the outlet, which are further used to calculate pressure gradient.

AlQuaimi and Rossen [21] used glass plates to build a variety of model fractures to study foam. Their models represent geological fractures and also easily facilitate the imaging study of in-situ foam. In our study, using similar methods, we create two model fractures, Model 1 and Model 2, with dimension 1 × 0.15 × 0.04 m (length × width × thickness). Each model is made of two 2-cm-thick glass plates (Hijman Glas B.V., the Netherlands). The top glass plate is smooth and the bottom plate is roughened on the side facing the top plate. The roughness of the bottom roughened plate is created by molding during the manufacturing process. The glass plates are strongly water-wet and the contact angle θ

is close to 0 °. To create a model, we place the smooth plate on top of the roughened plate and glue the edges using SR1–40B Silicon rubber. The model is then mounted in an aluminum clamping frame (Fig. 2). Due to limited penetration of glue along the edges, the two plates of each model are not directly against each other. The gap between the two plates represents a geological fracture. We drill in total six holes through the roughened plate for foam injection and discharge, and for linking to the pressure sensors. Two troughs (length × width × depth: $12 \times 2 \times 0.04$ cm) are milled in the rough plate. The one at the inlet facilitates a uniform foam injection into the fracture along its width. The one at the end of the model fracture prevents convergence of foam flow toward the outlet.

We use a high-speed micro-camera (Photron Fastcam UX50™, up to 160,000 fps) installed above the setup to visualize foam inside the model fractures and record its images. A back-light device (VAL LED lighting, VL-CB-CL), mounted under the fracture, provides high-parallelism white light for the camera. The entire setup is placed inside a black tent to avoid scattered light in order to improve the imaging quality.

In our experiments, we use a solution of 1 wt% AOS C14–16 surfactant (Stepan® BIO-TERGE AS-40 KSB, Active content: 39%, molecular weight: 324 g/mol) and nitrogen (Linde Gas Benelux B.V., Purity $\geq$ 99.999%) to create foam. The surface tension γ_s of the surfactant solution at 20 °C is 32.2 mN/m, measured by using a KSV Sigma™ Tensiometer.

3. Roughness and geometric characterization of model fractures

In our study, Model 1 and Model 2 have different roughness. Model 1 has roughness in a regular pattern, while Model 2 has roughness in an irregular pattern. Fig. 3 and Fig. 4 show relative height of the different roughened plates of Model 1 and Model 2, respectively. Although the roughness of Model 2 is irregular, a 20×20 mm profile of height (Fig. 4) is statistically representative along the whole roughened plate of Model 2 [21]. With a smooth plate on top, each model fracture provides a slit-like channel with variation in aperture for foam flow. Prior to foam injection, we measure hydraulic aperture of the fractures by injecting demineralized water (ELGA VEOLIA Labwater) through the pre-vacuumed fractures at stepwise-increasing volumetric rates. After water flow at each injection rate reaches steady-state, we record its pressure gradient. A regression of the pressure gradient against the injection rate determines the hydraulic aperture d_H of the model fracture [25]:

$$|\nabla P_w| = 12 \, q_w \frac{1}{w \, d_H^3} \, \mu_w \qquad (1)$$

where ∇P_w is the steady-state pressure gradient of water injection, q_w is the volumetric water rate, w is the width of the model fracture, and μ_w is water viscosity. The hydraulic aperture of Model 1 and Model 2 obtained from Eq. 1 are 46 and 78 μm, respectively.

In addition, we measure fracture volume of the two models by injecting demineralized water into the models (after firstly vacuuming) while closing the outlet valve. We stop the injection once the models are fully saturated with water: no remaining gas or vacuum spots have been detected. The volume of water injected by the pump is considered to be the fracture volume. In our study, the fracture volume of Model 1 and Model 2 are 9.1 mL and 14.2 mL, respectively. Using the value of fracture volume and relative height data of the roughened plate, we calculate aperture distribution of each model. Fig. 5 shows histogram of height data on the roughened plates and aperture distribution for the two model fractures.

With local hills (maxima of height) and valleys (minima of height) on the roughened plates, the distribution of aperture of both models can be represented as a 2D network of pore bodies and pore throats. Thus, with pore bodies and throats, the model fractures are comparable to the concept of microfluidic porous media. As shown in Fig. 3 and Fig. 4, we define pore bodies centered on local minima of height on the roughened plate, and pore throats, which connect pore bodies, at saddle points between pore bodies. The white dashed lines in Fig. 3 and Fig. 4 outline the boundaries we define as pore bodies. We then quantify typical apertures of pore bodies and pore throats. In Model 1, the definition of pore bodies is unambiguous. Each pore body has one local minimum of height and is connected to other four pore bodies through pore throats. In Model 2, our definition of pore bodies is less clear-cut: there may be multiple local minima (with only slightly different height) for each pore body on the roughened plate. We consider these to represent one pore body. Table 1 shows the spatial properties of our two model fractures, including pore density (number of pore bodies per unit area of roughened plate).

4. Coarsening experiments and image analysis

We conduct in total four experiments in the two model fractures (Table 2). Prior to each foam experiment, the model fracture is thoroughly cleaned by injecting 20 fracture pore volume of demineralized water, then vacuumed and fully saturated with surfactant solution. We pre-generate foam by injecting surfactant solution and gas through the mixing tee with an inside-mounted frit filter (mesh size: 10 μm) at foam qualities f_g (ratio of gas volumetric injection rate to total rate) 0.9 and 0.4 for both model fractures. The total interstitial velocity is 1.2 mm/s and 2 mm/s for Model 1 and Model 2, respectively (Table 2). The pre-generated foam is then injected into the horizontally-placed fracture without back-pressure. Despite considerable foam coarsening by
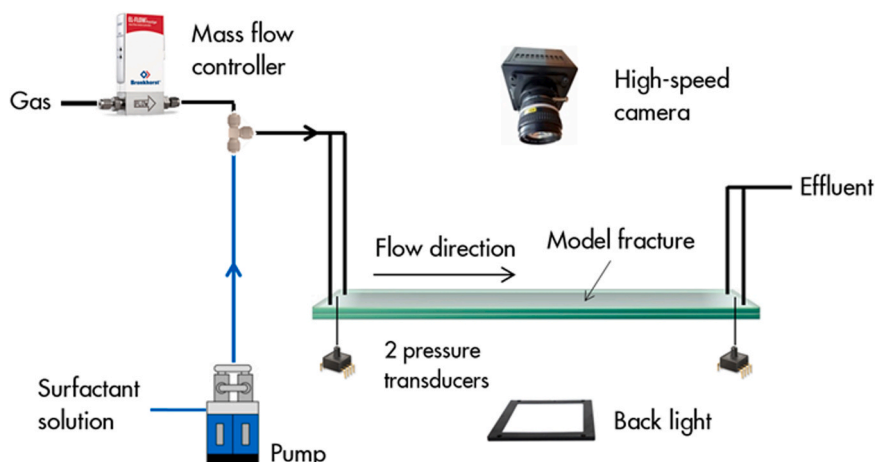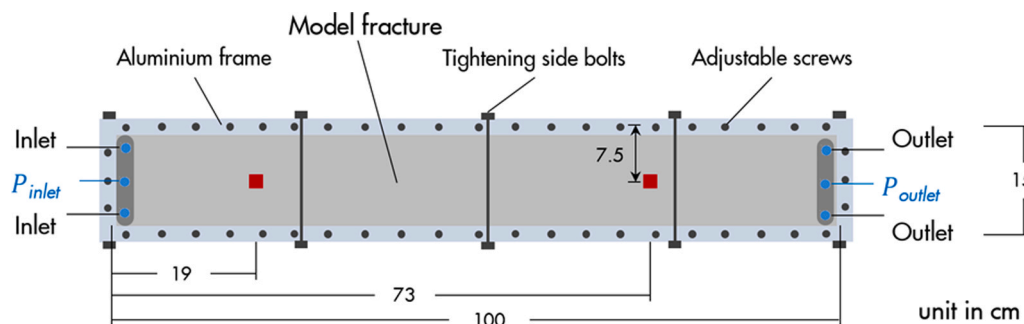

Fig. 1. Experimental setup.

Fig. 2. Horizontally-placed model fracture mounted in the aluminum clamping frame (top view). The red squares indicate the locations where images of foam shown in this study are recorded. For interpretation of the references to color in this figure legend, the reader is referred to the web version of this article.
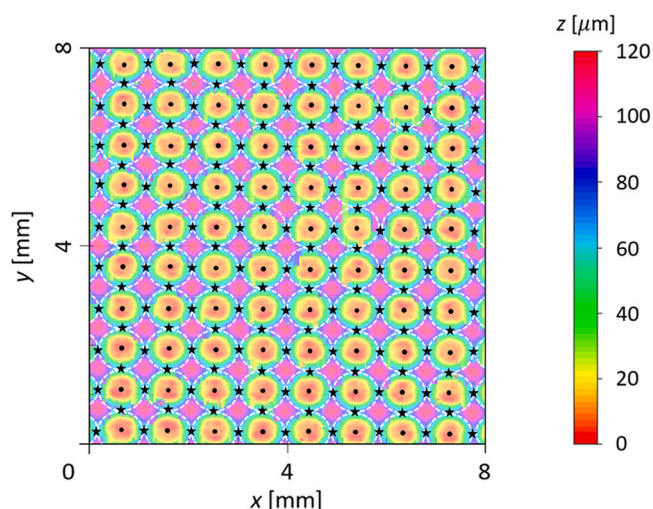

Fig. 3. Relative height of the roughened plate of Model 1 (regular pattern): resolution, 960 × 960; pixel size, 69 μm^2. The minimum height is set to 0 μm. Black stars are saddle points on the roughened plates, and black dots are local minima in height. The height data are profiled using a digital microscope (Keyence, VHX-7000™). White dashed lines outline the boundaries of pore bodies.
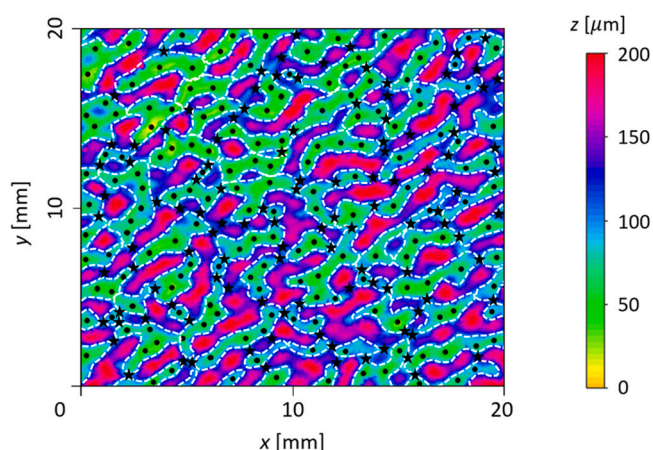

Fig. 4. Relative height of the roughened plate of Model 2 (irregular pattern): resolution, 2860 × 2860; pixel size, 49 μm^2. The minimum height is set to 0 μm. Black stars are saddle points on the roughened plates, and black dots are local minima in height. The height data are profiled using a digital microscope (Keyence, VHX-7000™). White dashed lines outline the boundaries of pore bodies.

diffusion between the mixing tee and the inlet of the fracture, the pre-generation step ensures that gas enters the fracture as relatively large bubbles instead of elongated gas slugs. Foam is further refined as it propagates through the model fracture due to in-situ bubble generation, mainly by lamella division [26]. After foam achieves steady-state, bubble generation and destruction rates are in local equilibrium in the second half of the model fracture [26]. In this study, the designed velocities ensure that foam reaches a stable pressure gradient, and they are not great enough to compromise the safety of our setup with glass model fractures. We maintain the steady-state injection for at least 1.5 h, and then close the inlet and outlet valves of the fracture. The model fracture is then shut in for 24 h at 20 °C.

Fig. 6 shows pressure gradient with foam in four experiments. The pressure gradient is calculated based on pressure drop from the inlet to the outlet of the model fractures. Time zero in Fig. 6 marks the beginning of foam injection into the fractures. In both model fractures, steady-state foam at foam quality 0.9 reaches a greater pressure gradient than foam quality 0.4. After shut-in, water and gas in foam flow along the model fractures to equalize pressure. At the beginning of the shut-in period, foam continues to flow, governed by a residual pressure gradient (Fig. 6). Once this pressure gradient drops below a value that can't compete with the yield stress of the foam, foam mostly stops flowing (0.08, 0.09, 0.10 and 0.12 h after the shut-in of the fractures for Experiments 1, 2, 3 and 4, respectively) and starts to coarsen due to diffusion between bubbles. As shown in Fig. 6, there is a small negative pressure gradient from the outlet toward the inlet of the fractures after foam stays at rest. As a result, during foam coarsening in our experiments, except Experiment 4, trains of bubbles occasionally flow in short bursts along separate pathways from outlet toward inlet. This evidently results from a small leak in the tubing upstream of the models. We also observed rare coalescence (rupture of lamellae) during convection of the bubble trains. However, the bubble texture wasn't much different after those intermittent periods of convection: the occasional convection of bubbles along separate pathways and coalescence of lamellae haven't significantly affected the overall behavior of foam coarsening in our study. Moreover, water in foam is transported along our models even during periods with no bubble flow.

To study these behaviors, we investigate foam at different locations in the model fractures and record the images of coarsening for 24 h at 4 frames per minute (see Table 2 for locations where images are recorded in each experiment). In this paper, we set time to zero at the point of shut-in, as the onset of our each coarsening experiment. As shown in Fig. 2, we record foam images at an upstream location 19 cm from fracture inlet, where foam is still relatively coarse-textured, and a downstream location 73 cm from the inlet, where foam is at local equilibrium (LE) before coarsening begins. At steady state with injected foam quality 0.9, LE foam at location 73 cm from the inlet has a bubble size (2D average bubble area) 23% and 38% smaller than the upstream foam at 19 cm in Models 1 and 2, respectively. ImageJ software is used to process raw foam images at different times of coarsening. In our two
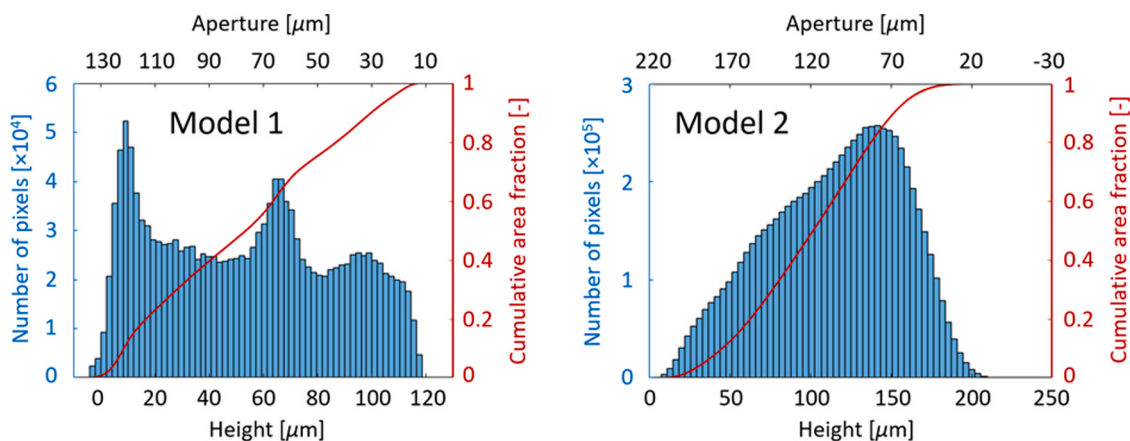
Fig. 5. Histogram of height of the roughened plate and aperture distribution of Model 1 (left) and Model 2 (right). Red curved lines are cumulative area fractions based on histogram of heights. For interpretation of the references to color in this figure legend, the reader is referred to the web version of this article.

Table 1
Spatial properties of Model 1 and Model 2.

	Hydraulic aperture, µm	Fracture volume, mL	Typical pore throat aperture, µm	Typical pore body aperture, µm	Pore density, /cm^2
Model 1 (regular roughness)	46	9.1	55	119	149
Model 2 (irregular roughness)	78	14.2	92	174	17

Table 2
Coarsening experiments conducted in this study and locations where foam images are recorded in the model fractures.

Experiment	Model fracture	Hydraulic aperture, µm	Total interstitial velocity, mm/s	Foam quality, -	Location where images are recorded (distance from fracture inlet), cm
1	Model 1 (regular roughness)	46	1.2	0.9	19 73
2	Model 1 (regular roughness)	46	1.2	0.4	73
3	Model 2 (irregular roughness)	78	2	0.9	19 73
4	Model 2 (irregular roughness)	78	2	0.4	73

Fig. 6. Pressure gradient of foam as a function of time since foam injection. Experiments 1 and 2 are conducted in Model 1 ($d_H = 46$ µm) at foam quality 0.9 and 0.4, respectively; Experiments 3 and 4 are conducted in Model 2 ($d_H = 78$ µm) at foam quality 0.9 and 0.4, respectively.

5. Estimation of water saturation and capillary pressure of foam in model fractures

In geological porous media, X-ray computed tomography (CT) is commonly used to map water saturation at different times of the foam process to evaluate its performance [27], [28]. However, capillary pressure is much more challenging to measure. In our model fractures, the capillary pressure in foam tends to equalize during the period of coarsening. The Plateau borders form an interconnected network for water to redistribute and capillary pressure to equalize, at least within the region of the image. Water-gas interfaces form at the edge of the water zones. The gap between the plates of the model fractures is much less than the radius of the water-gas interface as viewed from above. All water-gas interfaces are thus close to cylindrical. We assume that one interface would have the same local aperture d_a in the fracture as others within the area of an image due to nearly uniform capillary pressure in that area of the fracture. As shown in Fig. 8, water in foam in our model fractures resides in four locations: water zones that occupy locations of

model fractures, we observe only monolayer foam, with bubbles extending from top to bottom plates. Plateau borders form where lamellae meet the glass plates above and below. Fig. 7 shows raw and processed images of foam at 73 cm from the fracture inlet in Experiment 1 at a coarsening time 0.08 h. For each foam image, we distinguish the gas and water phases in the foam by tuning the threshold of the gray values of pixels. Gas bubbles and lamellae are thus identified in binary foam images. We quantify foam texture by measuring bubble density (number of bubbles per unit area of image) and bubble size (2D average bubble area). Unlike microfluidics with uniform depth of etching, our model fractures have a variation of aperture, with the presence of hills and valleys on the roughened plates (Fig. 3 and Fig. 4). As a result, there are local accumulations of water (water zones) that occupy locations of narrow aperture in the model fractures, governed by capillarity. We use ImageJ to calculate area fraction of these water zones and total length of lamellae $L_{lamella}$.
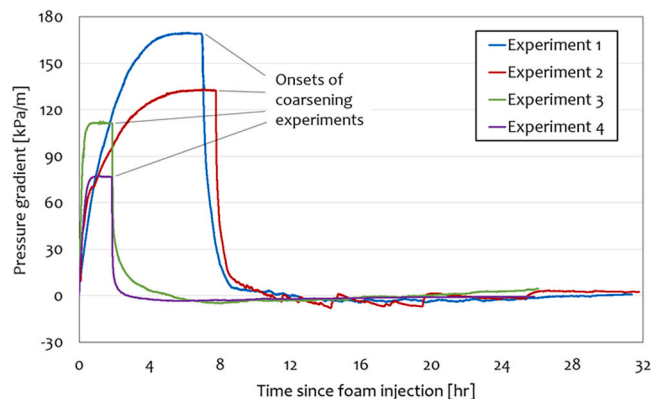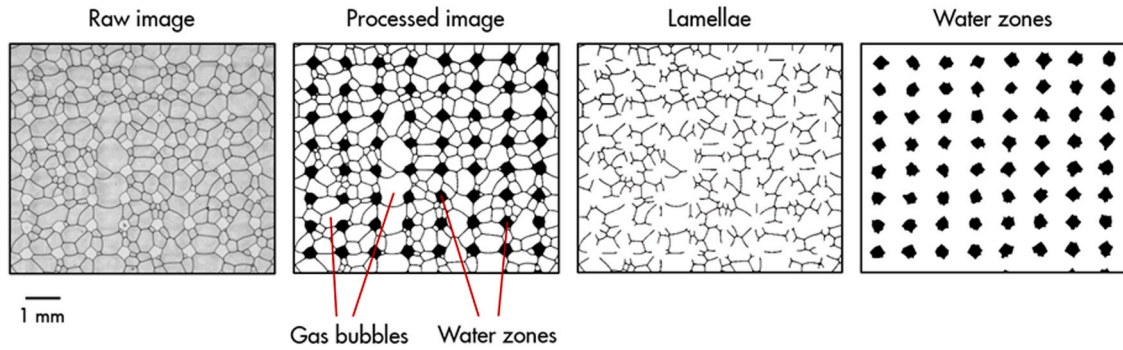
Fig. 7. Raw and processed images of foam in Model 1 at 0.08 h, image size: 7.8 × 6.8 mm. Water is shown in black, gas in white. Water zones occupy locations of narrow aperture in the model fracture.
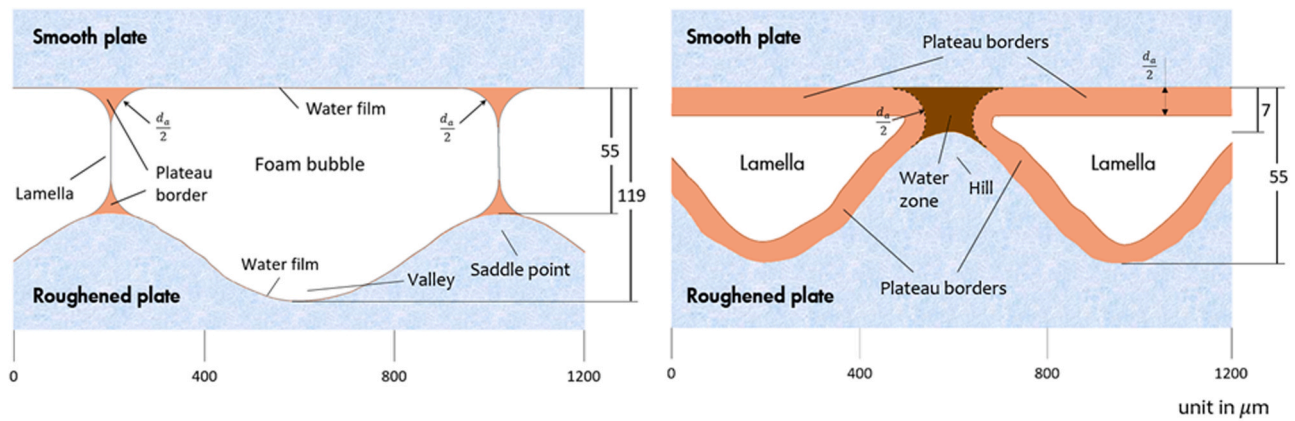

Fig. 8. Schematic of foam texture in Model 1 for a case where bubbles each fill a pore body. Left: cross-section view of gas bubbles in pore bodies, with lamellae in pore throats. Right: perpendicular view of lamellae and Plateau borders located at pore throats and water zone located at the location with tighter aperture. The vertical scale is greatly exaggerated.

narrow aperture, Plateau borders, lamellae between bubbles, and water films that wet glass walls above and below. The vertical scale in Fig. 8 is greatly exaggerated compared to the horizontal scale.

As lamellae and water films have a small thickness of 30 nm [29], [30], water zones of narrow aperture and Plateau borders thus account for almost all the water [24]. We use histogram of heights on the roughened plates (Fig. 3 and Fig. 4) to relate area fraction to volume of water in water zones. In addition, we relate aperture distribution in the model fractures and area fraction of water zones to estimate the local aperture d_a of water-gas interfaces. Using the value of aperture d_a, we estimate capillary pressure of foam P_c at a specific time of coarsening as:

$$P_c = \frac{2\,\gamma_s\,cos\theta}{d_a} \tag{2}$$

where γ_s is the surface tension of the surfactant solution, and θ is the contact angle. In this study, we assume that contact angle θ is 0, as water strongly wets the glass model fractures.

As shown in Fig. 8, under strongly water-wet conditions, as in our models, the radius of the Plateau borders is half of the local aperture of water-gas interfaces d_a. We calculate the volume of water in Plateau borders as:

$$V_{Pb} = (\frac{4-\pi}{4})\,d_a{}^2\,L_{lamella} \tag{3}$$

where $L_{lamella}$ is the sum of lengths of all lamellae in the image.

Combining water volume in Plateau borders with the volume of water zones in the image, we estimate water saturation of foam during coarsening. In addition, we estimate the height of the lamella surface that locates in a pore throat in the model fractures as $(d_{throat} - d_a)$, where

d_{throat} is the typical pore throat aperture of the model fractures (Table 1), and d_a is the local aperture of water-gas interfaces.

6. Results

6.1. Foam coarsening in two model fractures with different roughness

During coarsening in the model fractures, we also observed rare coalescence events (rupture of lamellae). However, the coalescence of lamellae hasn't significantly affected the overall behavior of foam coarsening in our study. Fig. 9 shows bubble density (number of bubbles per unit area of image) and bubble size (2D average bubble area) at different locations in the two model fractures during a 24-h coarsening period. These experiments are conducted at foam quality 0.9. In both model fractures, bubble density decreases and bubble size increases as foam coarsens. During coarsening, gas in bubbles at higher pressure diffuses through lamellae to bubbles at lower pressure. As a result, some bubbles disappear as all their gas diffuses into neighboring bubbles, and the remaining bubbles enlarge in size. As shown in Fig. 9, foam properties stay the same after 5 h in Model 1, indicating that coarsening stops. In Model 2, coarsening rate slows down after 18 h and bubble size still increases even up to 24 h. It implies an ongoing gas diffusion, though at a small rate.

As coarsening stops in Model 1 and slows down to a small rate after 18 h in Model 2, foam gains the same bubble texture at 19 cm as at 73 cm from the fracture inlet for both models. However, bubble size increases at greater rate in the first two hours at 19 cm than at 73 cm in both models, reflecting a greater coarsening rate. Fig. 10 shows bubbles per pore body as a function of coarsening time for the two models. After
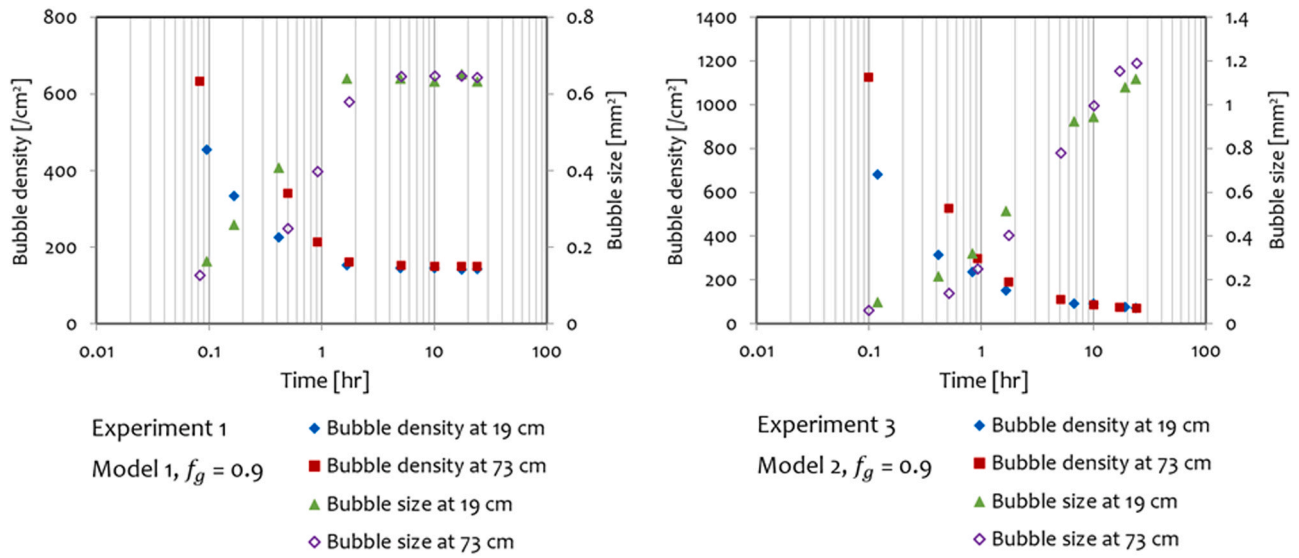
Fig. 9. Bubble density and bubble size at different locations during coarsening in Model 1 (left) and Model 2 (right). Foam is injected at foam quality 0.9.
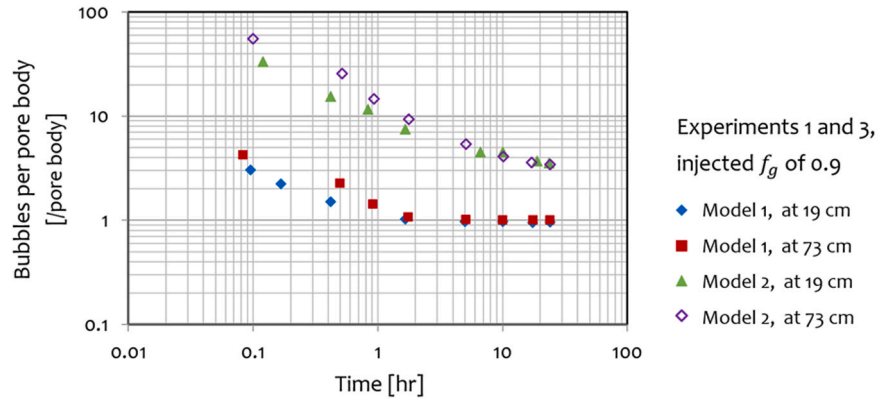

Fig. 10. Bubbles per pore body at different locations during coarsening in Models 1 and 2 (Experiments 1 and 3). Foam is injected at foam quality 0.9.
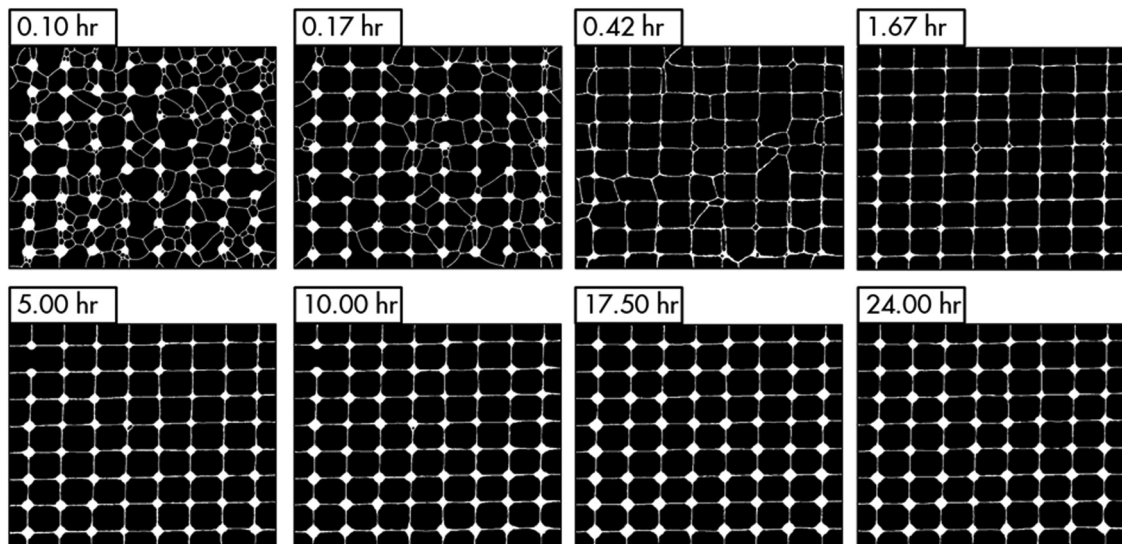

Fig. 11. Processed images of foam 19 cm from the fracture inlet, at different times of coarsening in Experiment 1 (in Model 1 with regular roughness, at foam quality 0.9), image size: 7.8 × 6.8 mm. Water is shown in white, gas in black.

coarsening stops in Model 1, there is one bubble in each pore. In Model 2, on average 3.3 bubbles stay in one pore after 24 h of coarsening. Unlike in Model 1, our definition of pore bodies in Model 2 is ambiguous, because there may be multiple local minima in height between well-defined pore boundaries (Fig. 4) in Model 2. It is possible that a lamella might locate at the saddle point between two of these minima, with zero curvature, at the end of the coarsening experiment.

Fig. 11 and Fig. 12 display processed images of foam at different times of coarsening at the two different locations in Model 1 with regular roughness (Experiment 1, at injected foam quality 0.9). Bubbles each attain the same size as the pore body as coarsening stops in Model 1. All lamellae then locate in pore throats with zero curvature. Although the lamella surface area at 24 h has an estimated height of 28 μm at position 19 cm, and up to 55 μm at position 73 cm in the fracture, coarsening stops, as all bubbles are in pressure equilibrium, with no driving force for gas diffusion.

Fig. 13 and Fig. 14 display processed foam images during coarsening at the two locations in Model 2 (Experiment 3, at injected foam quality 0.9). Compared to Model 1, Model 2 has a complex fracture geometry, due to its irregular roughness. In this fracture, a relatively small undulation in the bottom of a pore would not define a new pore. Therefore, it is challenging to conclude where lamellae locate in Model 2 after 24 h of coarsening, with multiple foam bubbles residing in one pore. During coarsening in the model fractures, foam bubbles restructure and lamellae relocate to achieve their minimum surface area. We therefore identify three types of lamella location in Model 2 at the end of Experiment 3: 1) in pore bodies, possibly at a local rise of height on the roughened plate: i.e., at the saddle point between two minima of height in the same pore body; 2) at pore throats; and 3) at locations of narrow aperture. We estimate the height of the lamella of case 1) as $(d_{body} - d_a)$, and that of case 2) as $(d_{throat} - d_a)$, where d_{body} and d_{throat} are the typical apertures of pore body and pore throat, respectively (Table 1), and d_a is the local aperture of water-gas interfaces. The estimated lamella heights of the first two cases are 112 and 30 μm for both locations at 19 and 73 cm from on Model 2. There would be gas diffusion through these lamellae if there were driving force. However, as shown in the bottom-right images (at 24 hr) of Fig. 13 and Fig. 14, the lamellae of cases 1) and 2) may not be moving at the end of the coarsening process in Experiment 3, as they are in positions of little or no curvature, with little or no driving force for diffusion. Lamellae of case 3) form the exposed sides of small bubbles wedged into locations of narrow aperture in Model 2, as shown in the red boxes in the bottom-right image of Fig. 14. Gas in these

small bubbles with greater curvature has higher pressure compared to the neighboring bubbles. However, they can remain in place for a considerable period of time. At these locations, the estimated height of these lamellae is close to 0. Thus there is little or no lamella surface area for gas diffusion.

Fig. 15 shows water saturation of foam during the 24-h coarsening period in the model fractures. Water saturation at the two locations of both models decreases as foam coarsens, except that water saturation first decreases and then slowly increases after 2 h at 19 cm in Model 1. The water saturation at 73 cm in Model 1 from 5 h of coarsening is not given in this paper. As shown in Fig. 12, as coarsening stops at 73 cm in Model 1 after 5 h, there are no local water-occupied zones at narrow apertures, and almost all water in foam locates in Plateau borders, at relatively high capillary pressure. It is then difficult to estimate the local aperture of water-gas interfaces, and from that the radius of Plateau borders, water saturation and capillary pressure. At the higher capillary pressure, the water saturation after 5 h is nevertheless at least lower than that at 1.75 h.

After the shut-in, this decrease of water saturation in both model fractures suggests that water continuously flows upstream into the inlet trough, tubing and fittings upstream of the model (Fig. 2) through the network of Plateau borders and water zones even without bubble flow, under the small pressure gradient from outlet toward inlet (Fig. 6). At 19 cm, the foam is drier compared to 73 cm for both model fractures. This explains why foam coarsens at a greater rate at 19 cm compared to 73 cm, as the drier foam has Plateau borders of smaller dimension under higher capillary pressure, and hence larger lamella surface area available for diffusion.

6.2. Foam coarsening at two different injected foam qualities

Fig. 16 compares bubbles per pore body during coarsening of foam injected at different foam qualities of 0.4 and 0.9 in the two models. These data are based on analysis at the location 73 cm from the fracture inlet. Fig. 17 and Fig. 18 display processed foam images at foam quality 0.4 at 73 cm in Models 1 and 2 (Experiments 2 and 4), respectively. In Model 1, the coarsening of both foams at foam qualities 0.4 and 0.9 stops at about 5 h, with one bubble occupying one pore. At injected foam quality 0.4, the estimated height of lamellae is 43 μm at the end of the coarsening. Similarly with foam at quality of 0.9, all these lamellae at quality of 0.4 also locate at pore throats with zero curvature at 24 h. There is no gas diffusion through these lamellae, and all bubbles are in
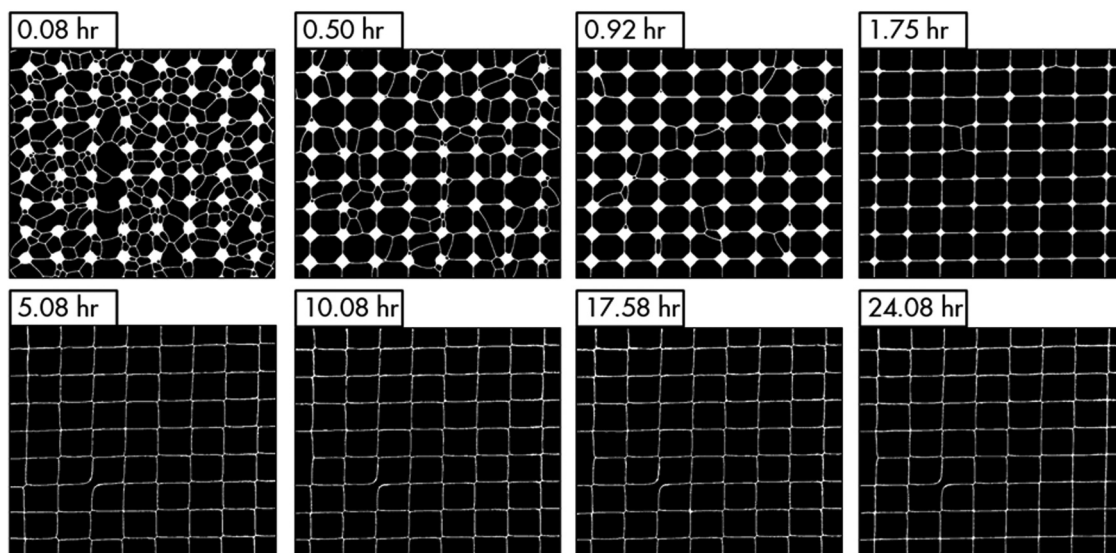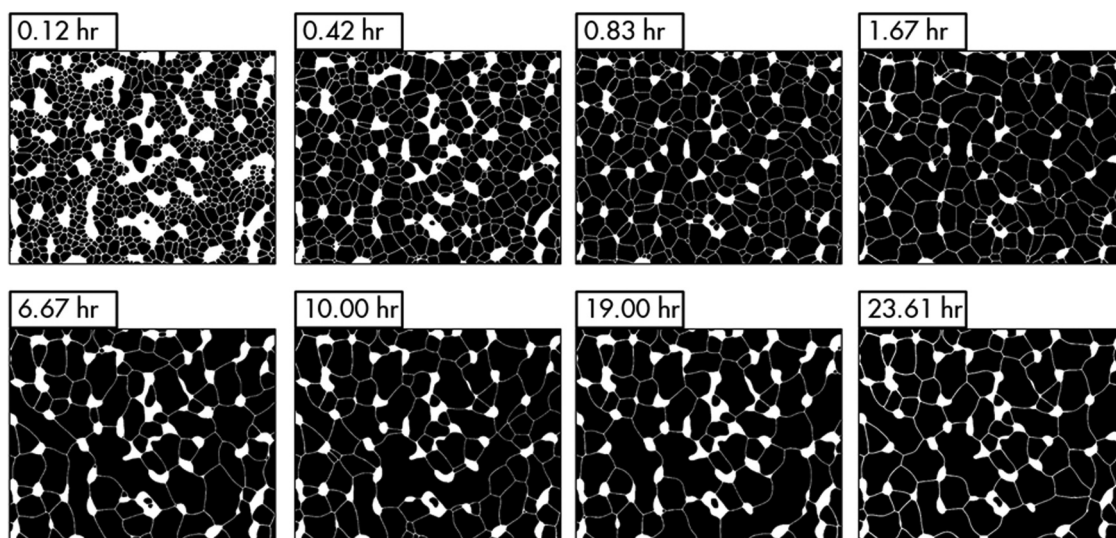

Fig. 12. Processed images of foam 73 cm from the fracture inlet, at different times of coarsening in Experiment 1 (in Model 1 with regular roughness, at foam quality 0.9), image size: 7.8 × 6.8 mm. Water is shown in white, gas in black.

Fig. 13. Processed images of foam 19 cm from the fracture inlet, at different times of coarsening in Experiment 3 (in Model 2 with irregular roughness, at foam quality 0.9), image size: 12.3 × 9.8 mm. Water is shown in white, gas in black.
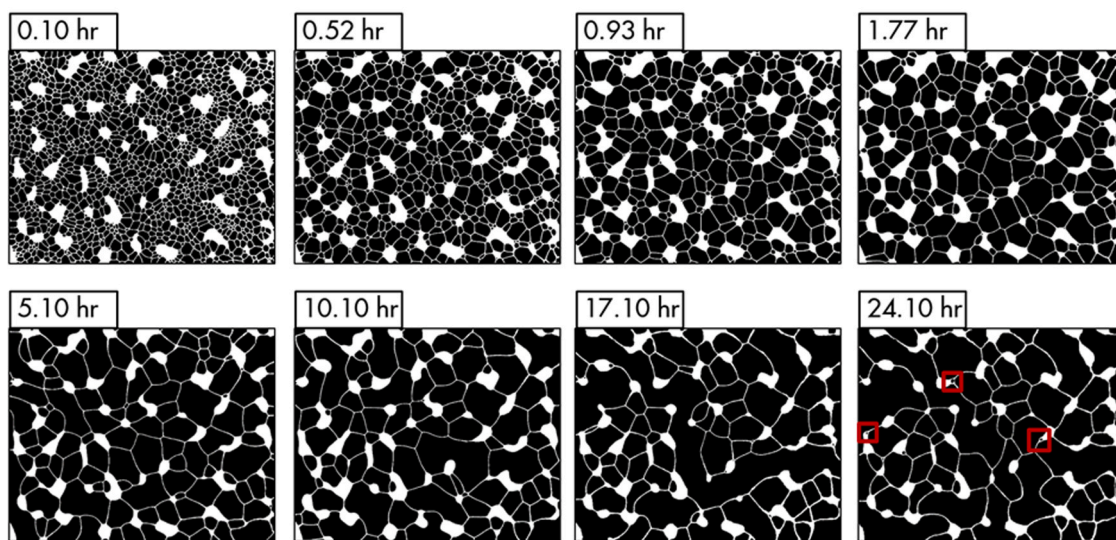

Fig. 14. Processed images of foam 73 cm from the fracture inlet, at different times of coarsening in Experiment 3 (in Model 2 with irregular roughness, at foam quality 0.9), image size: 12.3 × 9.8 mm. Water is shown in white, gas in black. Small bubbles in red boxes in the image at 24 h are in locations of narrow aperture in the model fracture.

equilibrium.

In Model 2, compared to foam quality 0.9, foam injected at quality of 0.4 coarsens at a slower rate. At the end of the coarsening experiment (at 24 hr), compared to 3.3 bubbles in one pore for foam injected at quality of 0.9, there are 6 bubbles for foam at quality of 0.4. Fig. 19 shows water saturation at different injected foam qualities at position 73 cm from fracture inlet during the 24-h coarsening period in the two model fractures. Water saturation at both foam qualities decreases as foam coarsens. During coarsening, water flows upstream into the inlet trough, tubing and fittings upstream of the model (Fig. 2) through Plateau borders and water zones under the small negative pressure gradient from the outlet toward the inlet of the fractures (Fig. 6). This pressure gradient evidently results from a small leak in the tubing upstream of the models. Fig. 20 shows capillary pressure as a function of water saturation of foam during coarsening at the location 73 cm from the fracture inlet in the two models. In both model fractures, the decrease in water saturation coincides with the increase in capillary pressure, as expected. The water saturation at foam quality 0.9 in Model 1 after 5 h of

coarsening is not given. There are no local water-occupied zones at locations of narrow apertures (Fig. 12). Almost all water in foam locates in Plateau borders. It is then difficult to estimate the local aperture of water-gas interfaces, and from that the radius of Plateau borders, water saturation and capillary pressure. It is evident that the out-flow water rate is greater than the in-flow water rate at position 73 cm from the inlet of Model 1. The water saturation after 5 h there is at least lower than that at 1.7 h, with greater capillary pressure.

At wetter conditions, the local aperture at water-gas interfaces in the fracture is larger, due to the lower capillary pressure. The Plateau borders of foam therefore are larger, and the height of lamellae between bubbles is smaller. Compared to dry foams, this lack of lamellae in wet foams slows gas diffusion: hence the slower coarsening at foam quality 0.4. Similarly with foam at quality 0.9, lamellae of foam at quality 0.4 also stay in three locations of narrow aperture in Model 2 at the end of the coarsening experiment (bottom-right image in Fig. 18). However, the lamellae have smaller heights there: lamellae of case 1) possibly locate at a local rise of height in pore bodies. They have little or no
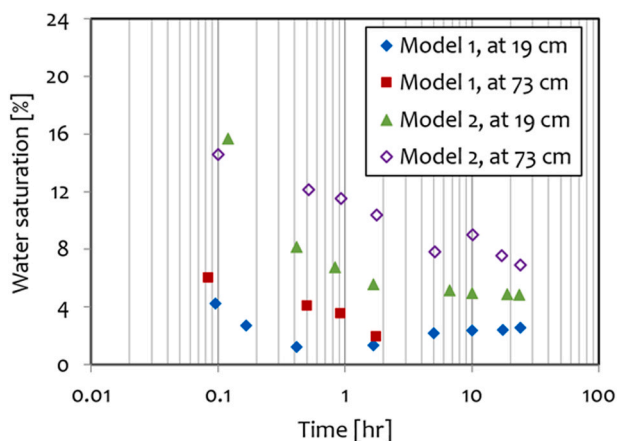
Fig. 15. Water saturation of foam at different locations during coarsening in Model 1 and Model 2. Foam is injected at foam quality 0.9.

curvature with an estimated height of 80 μm; Lamellae of case 2) locate at pore throats and have an estimated height close to 0; and lamellae of case 3) form the exposed sides of small bubbles (as shown in the red

boxes in the bottom-right image of Fig. 18) at narrow aperture in Model 2. The estimated height of lamellae of this case is also close to 0. The gas diffusion rate through lamellae of all three cases is thus either zero or much weak at the end of the coarsening experiment.

7. Discussion

In this paper, we have reported an experimental coarsening study of foam in two model fractures. Unlike microfluidic models with uniform depth of etching, our slit-like open fractures each have a distribution of apertures in space. Because of this variation, foam coarsening stops or reaches an insignificant rate, as all lamellae move in locations with local minima in surface area, such as pore throats or local saddle points between two minima of heights in pore bodies. Coarsening rate approaches zero for bubbles at locations of narrow aperture (local hills on the roughened plates) because lamellae area approaches zero. Fracture models built with two smooth plates (without roughness) with a hydraulic aperture of tens of microns to millimeters have been used to study foam [31–34]. We expect that static foam would coarsen into one large bubble in such models after a period of time, because with uniform aperture there are no locations with local minimum in lamella area.

In 2D foams, the coarsening is generally described using von Neumann's law, by assuming that foam is confined in an infinite 2D space
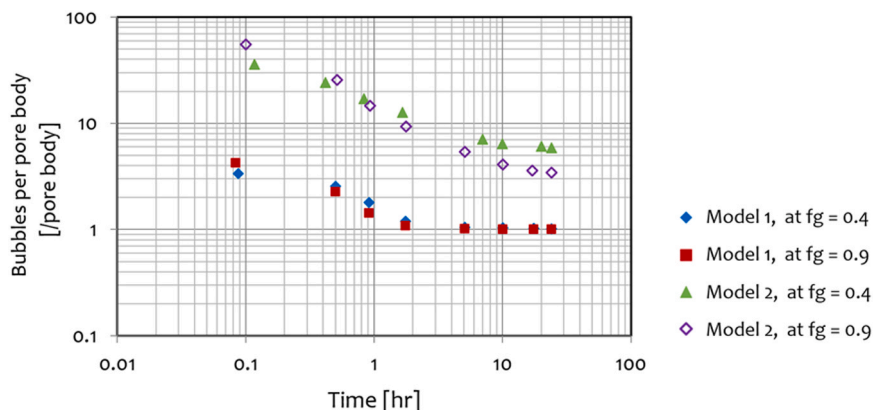

Fig. 16. Bubbles per pore body during coarsening at different injected foam qualities in Models 1 and 2. Data are based on foam analysis at 73 cm from the fracture inlet.
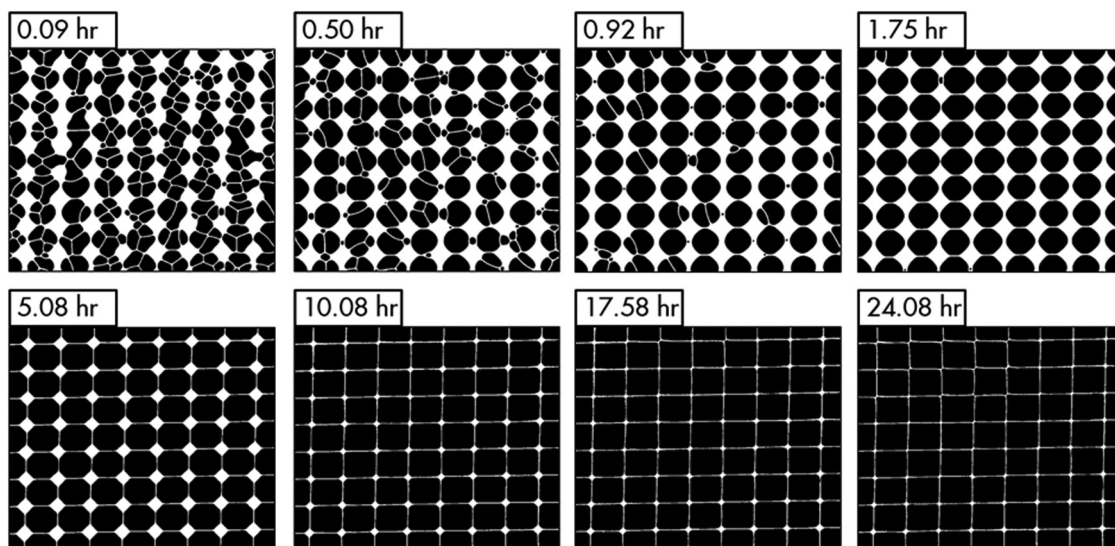

Fig. 17. Processed images of foam 73 cm from the fracture inlet, at different times of coarsening in Experiment 2 (in Model 1 with regular roughness, at foam quality 0.4), image size: 7.8 × 6.8 mm. Water is shown in white, gas in black.
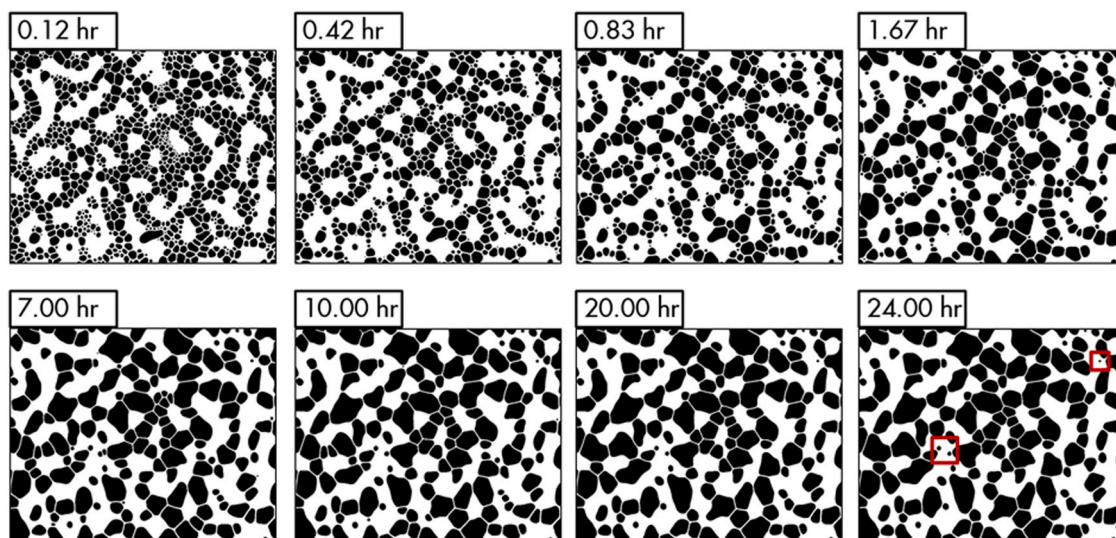
Fig. 18. Processed images of foam 73 cm from the fracture inlet, at different times of coarsening in Experiment 4 (in Model 2 with irregular roughness, at foam quality 0.4), image size: 12.3 × 9.8 mm. Water is shown in white, gas in black. Small bubbles in red boxes in the image at 24 h are in locations of narrow aperture in the model fracture.
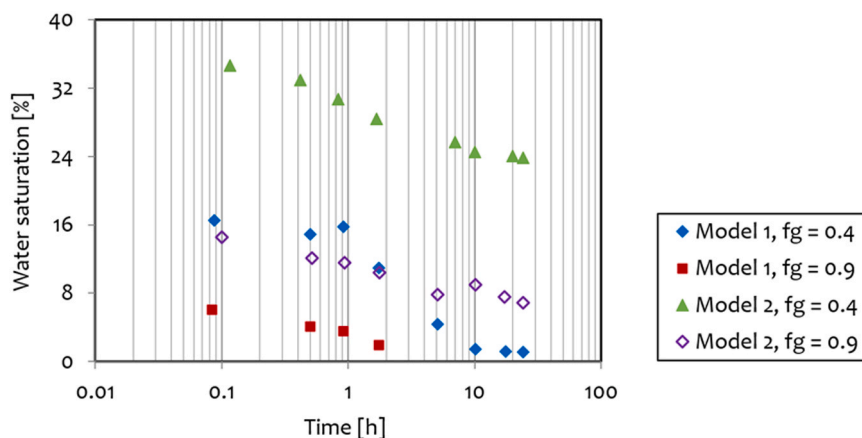

Fig. 19. Water saturation of foam at different injected foam qualities during coarsening in Model 1 and Model 2. Data are analyzed at the position 73 cm from fracture inlet.
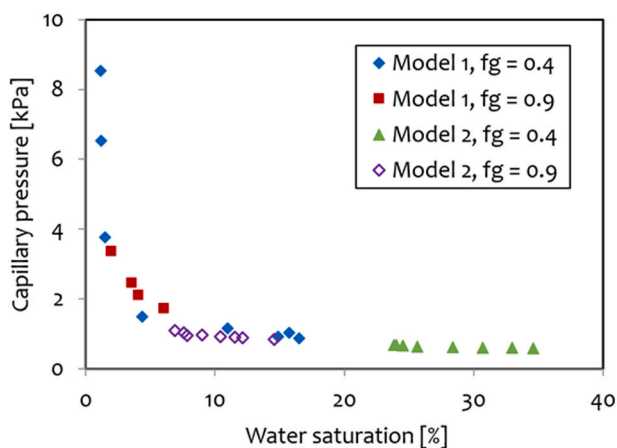

Fig. 20. Capillary pressure as a function of water saturation of foam in the two model fractures.

and bubbles are separated by lamellae with the same height [35], [36, 37]. In our models, the fracture aperture distribution fundamentally affects the coarsening behavior. The structure of foam is complex, with some water accumulated in locations of narrow aperture in the models. Therefore, it is difficult to formulate a scaling law to predict coarsening behavior in our model fractures. As an initial study, we adopted an image-analysis technique to relate the fracture geometries and foam bubble properties. In particular, we estimate the height of lamellae based on their locations in the model fractures, to study the coarsening process.

The network of Plateau borders and water zones acts as the paths for water to flow in and out along our fractures during coarsening. Although water zones are mostly narrower in aperture than the Plateau borders, they are much wider in area. This geometry suggests that the water zones have essentially no resistance to flow compared to other parts of the network. In the fractures, the total water saturation, which includes water zones and Plateau borders, is related to capillary pressure. Water is apparently transported from one side of the fractures to the other to equalize the difference in capillary pressure. The implication of the flow conductivity of the network on this water transport behavior deserves further study.

8. Conclusions

In this study, we have built two 1-meter-long glass model fractures with different roughness and hydraulic apertures to study coarsening behavior of foam. We found that bubble density decreases and average bubble size (2D average bubble area) increases as foam coarsens in both model fractures. In Model 1 with regular roughness, coarsening stops and bubbles are in equilibrium after 5 h. Each bubble then occupies one pore body and all lamellae remain at pore throats with zero curvature. However, foam continues to coarsen up to 24 h in Model 2 with irregular roughness, although at a greatly-reduced rate. At the end of the coarsening experiments, either lamellae are in positions of little or no curvature, or the exposed sides of small bubbles wedged into locations of narrow aperture in Model 2 have an estimated lamella height close to zero. During coarsening in both model fractures, water flows in and out along the fractures following the network of Plateau borders and water zones at narrow apertures. At the two fixed locations in the fractures where we take images, water saturation decreases as foam coarsens, which coincides with an increase in capillary pressure. Compared to foam injected at a lower foam quality, foam at a higher quality coarsens faster. In drier foam, the Plateau borders are smaller in size at higher capillary pressure. The height of lamellae is thus greater, hence allowing faster gas diffusion.

CRediT authorship contribution statement

Kai Li: Conceptualization, Methodology, Software, Writing – original draft, Writing – review & editing. **Mohammadamin Sharifnik:** Software. **Karl-Heinz A.A. Wolf:** Methodology, Supervision, Writing – review & editing. **William R. Rossen:** Conceptualization, Methodology, Supervision, Writing – review & editing.

Declaration of Competing Interest

The authors declare that they have no known competing financial interests or personal relationships that could have appeared to influence the work reported in this paper.

Data availability

The data sets reported in this study are available from the corresponding author.

References

[1] Gauglitz, P.A., Friedmann, F., Kam, S.I., and Rossen, W.R. 2002, April. Foam generation in porous media. In SPE/DOE Improved Oil Recovery Symposium. OnePetro. ⟨https://doi.org/10.2118/75177-MS⟩.

[2] Hirasaki, G.J., Miller, C.A., Szafranski, R., Lawson, J.B., and Akiya, N. 1997. Surfactant/foam process for aquifer remediation. In International symposium on oilfield chemistry. SPE 37257-MS. ⟨https://doi.org/10.2118/37257-MS⟩.

[3] K.E. Thompson, R.D. Gdanski, Laboratory study provides guidelines for diverting acid with foam, SPE Prod. Facil. 8 (04) (1993) 285–290, https://doi.org/10.2118/23436-PA.

[4] A.R. Kovscek, C.J. Radke, Fundamentals of foam transport in porous media, in: L. L. Schramm (Ed.), Amer. Chem. Soc., 242, Foams in the Petroleum Industry, Washington, D.C., 1994, pp. 115–163.

[5] Rossen, W.R. 1996. Foams in enhanced oil recovery in Foams: Theory, Measurements, and Application, ed. Prud'homme, Robert K., 57, 413–464.

[6] Lake, L.W., Johns, R.T., Rossen W.R., and Pope, G.A. 2014. Fundamentals of Enhanced Oil Recovery, Society of Petroleum Engineers, Richardson, TX.

[7] Boud, D.C. and Holbrook, O.C. 1958. U.S. Patent No. 2,866,507. Washington, DC: U.S. Patent and Trademark Office.

[8] Fried, A.N, The Foam-Drive Process for Increasing the Recovery of Oil. US Bureau of Mixes, Rep. Inv, 5866, 1961.

[9] G.C. Bernard, L.W. Holm, C.P. Harvey, Use of surfactant to reduce CO_2 mobility in oil displacement, Soc. Pet. Eng. J. 20 (04) (1980) 281–292, https://doi.org/10.2118/8370-PA.

[10] Farajzadeh, R., Wassing, B., and Boerrigter, P. 2010, September. Foam assisted gas oil gravity drainage in naturally-fractured reservoirs. In SPE Annual Technical Conference and Exhibition. ⟨https://doi.org/10.2118/134203-MS⟩.

[11] G.J. Hirasaki, J.B. Lawson, Mechanisms of foam flow in porous media: apparent viscosity in smooth capillaries, Soc. Pet. Eng. J. 25 (02) (1985) 176–190, https://doi.org/10.2118/12129-PA.

[12] S. Cohen-Addad, H. Hoballah, R. Höhler, Viscoelastic response of a coarsening foam, Phys. Rev. E 57 (6) (1998) 6897–6901, https://doi.org/10.1103/PhysRevE.57.6897.

[13] D.L. Weaire, S. Hutzler, The Physics of Foams, Oxford University Press, 2001.

[14] D. Weaire, The rheology of foam, Curr. Opin. Colloid Interface Sci. 13 (3) (2008) 171–176, https://doi.org/10.1016/j.cocis.2007.11.004.

[15] I. Cantat, S. Cohen-Addad, F. Elias, F. Graner, R. Höhler, O. Pitois, F. Rouyer, A. Saint-Jalmes, Foams: Structure and Dynamics, OUP Oxford, 2013.

[16] C. Monnereau, M. Vignes-Adler, Dynamics of 3D real foam coarsening, Phys. Rev. Lett. 80 (23) (1998) 5228–5231, https://doi.org/10.1103/PhysRevLett.80.5228.

[17] A. Saint-Jalmes, D. Langevin, Time evolution of aqueous foams: drainage and coarsening, J. Phys.: Condens. Matter 14 (40) (2002) 9397–9412.

[18] S. Hilgenfeldt, S.A. Koehler, H.A. Stone, Dynamics of coarsening foams: accelerated and self-limiting drainage, Phys. Rev. Lett. 86 (20) (2001) 4704–4707, https://doi.org/10.1103/PhysRevLett.86.4704.

[19] Marchalot, J., Lambert, J., Cantat, I., Tabeling, P., and Jullien, M.C. 2008. 2D foam coarsening in a microfluidic system. EPL (Europhysics Letters), 83(6), 64006. DOI: ⟨10.1209/0295–5075/83/64006⟩.

[20] S.A. Jones, N. Getrouw, S. Vincent-Bonnieu, Foam flow in a model porous medium: I. The effect of foam coarsening, Soft Matter 14 (18) (2018) 3490–3496, https://doi.org/10.1039/C7SM01903C.

[21] B.I. AlQuaimi, W.R. Rossen, Foam generation and rheology in a variety of model fractures, Energy Fuels 33 (1) (2018) 68–80, https://doi.org/10.1021/acs.energyfuels.8b02178.

[22] Buchgraber, M., Castanier, L.M., and Kovscek, A.R. 2012, October. Microvisual investigation of foam flow in ideal fractures: role of fracture aperture and surface roughness. In SPE Annual Technical Conference and Exhibition. OnePetro. ⟨https://doi.org/10.2118/159430-MS⟩.

[23] J. Gauteplass, K. Chaudhary, A.R. Kovscek, M.A. Fernø, Pore-level foam generation and flow formobility control in fractured systems, Colloids Surf. A: Physicochem. Eng. Asp. 468 (2015) 184–192, https://doi.org/10.1016/j.colsurfa.2014.12.043.

[24] Li, K., Wolf, KH.A. A., and Rossen, W.R. 2021. A Novel Technique to Estimate Water Saturation and Capillary Pressure of Foam in Model Fractures. Submitted to Colloids and Surfaces A: Physicochemical and Engineering Aspects. COLSUA-D-21–02626.

[25] P.A. Witherspoon, J.S. Wang, K. Iwai, J.E. Gale, Validity of cubic law for fluid flow in a deformable rock fracture, Water Resour. Res. 16 (6) (1980) 1016–1024, https://doi.org/10.1029/WR016i006p01016.

[26] K. Li, K.H.A.A. Wolf, W.R. Rossen, Effects of gas trapping on foam mobility in a model fracture, Transp. Porous Media 138 (2021) 185–200, https://doi.org/10.1007/s11242-021-01598-y.

[27] Tang, J., Vincent-Bonnieu, S., and Rossen, W.R. 2019, September. CT Coreflood Study of Transient Foam Flow with Oil. In SPE Annual Technical Conference and Exhibition. Society of Petroleum Engineers. ⟨https://doi.org/10.2118/196202-MS⟩.

[28] J. Gong, S. Vincent-Bonnieu, R.Z. Kamarul Bahrim, C.A. Che Mamat, R.D. Tewari, M.I. Mahamad Amir, W.R. Rossen, Injectivity of multiple slugs in surfactant alternating gas foam EOR: A CT scan study, SPE J. 25 (2020) 895–906, https://doi.org/10.2118/199888-PA.

[29] G.J. Hirasaki, Wettability: fundamentals and surface forces, SPE Form. Eval. 6 (02) (1991) 217–226, https://doi.org/10.2118/17367-PA.

[30] V. Bergeron, C.J. Radke, Equilibrium measurements of oscillatory disjoining pressures in aqueous foam films, Langmuir 8 (12) (1992) 3020–3026, https://doi.org/10.1021/la00048a028.

[31] Pieters, D.A. and Graves, R.M. 1994, October. Fracture relative permeability: linear or non-linear function of saturation. In International Petroleum Conference and Exhibition of Mexico. OnePetro. ⟨https://doi.org/10.2118/28701-MS⟩.

[32] C.Y. Chen, R.N. Horne, M. Fourar, Experimental study of liquid-gas flow structure effects on relative permeabilities in a fracture, Water Resour. Res. 40 (8) (2004), https://doi.org/10.1029/2004WR003026.

[33] W. Yan, C.A. Miller, G.J. Hirasaki, Foam sweep in fractures for enhanced oil recovery, Colloids Surf. A: Physicochem. Eng. Asp. 282 (2006) 348–359, https://doi.org/10.1016/j.colsurfa.2006.02.067.

[34] B. Géraud, S.A. Jones, I. Cantat, B. Dollet, Y. Méheust, The flow of a foam in a two-dimensional porous medium, Water Resour. Res. 52 (2) (2016) 773–790, https://doi.org/10.1002/2015WR017936.

[35] J. von Neumann, Metal interfaces, Am. Soc. Met. Clevel. 108 (1952).
[36] J.A. Glazier, S.P. Gross, J. Stavans, Dynamics of two-dimensional soap froths, Phys. Rev. A 36 (1) (1987) 306–312, https://doi.org/10.1103/PhysRevA.36.306.

[37] M. Emília Rosa, M.A. Fortes, Coarsening of two-dimensional foams confined by walls, Philos. Mag. A 79 (8) (1999) 1871–1886, https://doi.org/10.1080/01418619908210397.